Journal of Computational Physics 229 (2010) 6193–6207

Contents lists available at ScienceDirect

Journal of Computational Physics

journal homepage: www.elsevier.com/locate/jcp

Finite element modeling of the deformation of magnetoelastic film ☆

Matthew I. Barham [a], Daniel A. White [a,*], David J. Steigmann [b]

[a] Lawrence Livermore National Laboratory, 7000 East Avenue, Livermore, CA 94551, United States
[b] 6133 Etcheverry Hall, University of California, Berkeley, CA 94720, United States

ARTICLE INFO

Article history:
Received 28 May 2009
Received in revised form 2 April 2010
Accepted 7 April 2010
Available online 29 April 2010

Keywords:
Magnetoelastic
Magnetics
Deformation
Finite element

ABSTRACT

Recently a new class of biocompatible elastic polymers loaded with small ferrous particles, a magnetoelastic polymer, has been developed. This engineered material is formed into a thin film using spin casting. An applied magnetic field will deform the film. The magnetic deformation of this film has many possible applications, particularly in microfluidic pumps and pressure regulators. In this paper a finite element method suitable for the transient simulation of arbitrarily shaped three-dimensional magnetoelastic polymers subjected to time-varying magnetic fields is developed. The approach is similar to that employed in finite elment magnetohydrodynamic simulations, the key difference is a more complex hyperelastic material model. In order to confirm the validity of the approach, finite element solutions for an axially symmetric thin film are compared to an analytical solution based on the membrane (infinitely thin) approximation. For this particular problem the two approaches give qualitatively similar results and converge as the film thickness approaches zero.

Published by Elsevier Inc.

1. Introduction

The motivation for this work stems from the creation of thin magnetoelastic films. The magnetoelastic material consists of a mixture of iron powder, polydimethylsiloxane (PDMS), and surfactants. The surfactant is used to increase dispersion of the iron particles. Excellent mixing is a requirement to optimize the dispersion of the iron into the PDMS matrix and to break up large iron agglomerates. The material is formed into a thin film using spin casting. Some possible applications of magnetoelastic films include microfluidic actuators [1] and environmental sensors [2–4].

The basic equilibrium theory for magnetoelastic materials can be found in, for example, [5–7]. In these works the energy, stress, and variational principles are derived. There are differences depending upon the choice of primary fields, but for particular choices the net result is that the total system stress tensor can be written in terms of the elastic Cauchy stress tensor [8] that is independent of the magnetic field, plus a Maxwell stress tensor [9] that is independent of displacement. Since finite element methods for elasticity and magnetics exist, the total system stress tensor concept points the way to a fully-coupled magnetoelastic finite element method.

The goal of the work presented here is to develop a computational procedure for the simulation of arbitrarily shaped three-dimensional magnetoelastic films subjected to a transient magnetic field. An unstructured mesh is used to represent the geometry, a finite element method is used for the spatial discretization, and implicit finite difference methods are used for the temporal discretization. The elastic equations are solved for the material deformation, the magnetic equations are

☆ This work was performed under the auspices of the US Department of Energy by the University of California, Lawrence Livermore National Laboratory under contract DE-AC52-07NA27344.

* Corresponding author. Tel.: +1 925 422 9870.
E-mail address: white37@llnl.gov (D.A. White).

0021-9991/$ - see front matter Published by Elsevier Inc.
doi:10.1016/j.jcp.2010.04.007

solved for the magnetic fields in both the material region and the large but finite volume of surrounding space. The surrounding space contains coils used to generate the time-dependent magnetic field. The magnetic equations are not magnetostatic, but rather a time-dependent diffusion equation, i.e. eddy current equation. This is important if the time dependence of the external field is fast enough (e.g. kilohertz) to generate eddy currents. The time-dependent diffusion equation developed here does converge to the magnetostatic solution for steady-state problems. The elastic equations and the magnetic equations are solved in an operator split manner. This approach has successfully been used in magnetohydrodynamic (MHD) simulations [10]. Some key differences for this magnetoelastic application, compared to the MHD application, are that a hyperelastic Mooney–Rivlin model is used for the PDMS material constitutive relation, and the time scale warrants an unconditionally stable implicit time integration method.

In order to confirm the validity of the approach, finite element solutions are compared to an analytical solution for the special case of a thin axially symmetric magnetoelastic film in a static dipole field. The analytical method is based on the *membrane approximation*, the aspect ratio between the thickness and radius of the film is small, thus taking the leading order terms of an asymptotic expansion leads to a model where rigidity with respect to bending is neglected [11]. In the limit as the film thickness approaches zero and the deformation approaches steady-state, the finite element solution to approaches the analytical solution, providing an important verification of the finite element implementation.

In Section 2 the finite element formulations is discussed including subsections on the governing partial differential equations, variational statement, finite element basis functions, time integration, mesh relaxation and solution process. Section 3 gives an outline of the analytic model used for comparison. Section 4 presents the values used for the calculation and the results. A conclusion is provided in Section 5.

2. Finite element formulation

2.1. Governing partial differential equations

We begin by briefly reviewing various formulations for time-dependent low-frequency electromagnetics, i.e. the diffusion or eddy current approximation. Maxwell's equations involve the electric ($\vec{E}$) and magnetic ($\vec{H}$) fields, the electric ($\vec{D}$) and magnetic ($\vec{B}$) flux densities, and the current density $\vec{J}$. These quantities are not independent but are related to each other through the constitutive relations $\vec{D} = \epsilon\vec{E}$, $\vec{B} = \mu\vec{H}$, and $\vec{J} = \sigma\vec{E}$ where ϵ is the dielectric permittivity, μ is the magnetic permeability, and σ is the electrical conductivity. Since there are divergence constraints

$$\vec{\nabla}\cdot\vec{J} = 0, \tag{1}$$

$$\vec{\nabla}\cdot\vec{B} = 0, \tag{2}$$

it is sometimes convenient to introduce the magnetic ($\vec{A}$) and electric ($\vec{T}$) vector potentials such that

$$\vec{B} = \vec{\nabla}\times\vec{A}, \tag{3}$$

$$\vec{J} = \vec{\nabla}\times\vec{T}, \tag{4}$$

and in order to uniquely define $\vec{A}$ and $\vec{T}$ gauge conditions need to be applied to these vector potentials. Depending upon the chosen gauge conditions additional electric (Φ_E) and magnetic (Φ_H) scalar potentials may be introduced. The redundancy of the fields and arbitrariness of gauge conditions leads to a great variety of finite element formulations for electromagnetics. An example of an $\vec{E}$-field formulation can be found in [12], in this formulation the electric field is the only variable. Examples of the $\vec{H}$-field formulation can be found in [13,14], in this formulation the magnetic field is the only variable. Examples using the magnetic vector potential and the electric scalar potential, the so-called $\vec{A}-\Phi$ formulation, can be found in [15–17]. It has been shown in [18] that, when using $H(Curl)$-conforming basis functions, these three formulations give identical results, the only difference is that the different methods require different boundary to be provided. Yet another formulation uses the electric vector potential and the magnetic scalar potential, the so-called $\vec{T}-\Omega$ formulation, as described in [19]. This approach supposedly has advantages for problems in which only a small portion of the entire problem is conducting.

The approach used here is to work with the primary fields rather than with vector potentials. A combined $\vec{E}-\vec{B}$ formulation is used, i.e. the electric field and the magnetic flux density are both computed. This approach is used because a magnetic field is required for computation of magnetic forces, and the electric field facilitates coupling with external circuits [20]. And a pragmatic reason is that we are building upon an existing magnetohydrodynamic code [10] that uses $\vec{E}$ and $\vec{B}$ as the variables. The key electromagnetic partial differential equations are then

$$\vec{\nabla}\cdot\sigma\vec{\nabla}\Phi_E = 0, \tag{5}$$

$$\sigma\vec{E}_{ind} = \vec{\nabla}\times\frac{1}{\mu}\vec{B} + \sigma\vec{\nabla}\Phi_E, \tag{6}$$

$$\frac{\partial\vec{B}}{\partial t} = -\vec{\nabla}\times\vec{E}_{ind}, \tag{7}$$

$$\overline{T}_M = \frac{1}{\mu}\vec{B}\otimes\vec{B} - \frac{1}{2\mu}\left(\vec{B}\cdot\vec{B}\right)\bar{I}, \tag{8}$$

where the first equation is a Poisson's equation for the electrostatic potential, the second equation is Ampere's law (neglecting displacement current, i.e. the eddy current approximation), and the third equation is Faraday's law. The electrostatic potential (Φ_E) is used to drive current into a coil, if a coil is present in the problem. In (6) $\vec{E}_{ind}$ is the induced, or solenoidal, component of the electric field. As mentioned previously there are also divergence constraints on the electromagnetic quantities (1) and (2). These divergence constraints can be satisfied by proper choice of finite element basis functions.

The above electromagnetic equations are coupled with the Cauchy equation of motion via the total stress tensor $\overline{T}$,

$$\rho \frac{d^2\vec{u}}{dt^2} = \vec{\nabla} \cdot \overline{T} + \rho\vec{b}, \tag{9}$$

$$\overline{T} = \overline{T}_C + \overline{T}_M. \tag{10}$$

In (9) ρ is the density, $\vec{u}$ is the displacement, $\overline{T}$ is the total stress tensor, and $\vec{b}$ is a body force (e.g. gravity). Note that (9) is derived by combining conservation of linear momentum with conservation of mass. Conservation of angular momentum is also satisfied by (9) when the stress tensor is symmetric. For the magnetoelastic film application the Cauchy stress tensor will be given by the nonlinear hyperelastic Mooney–Rivlin model. In this model the stress $\overline{T}_C$ is a function of the displacement $\vec{u}$. The functional form is complicated and requires some further definitions.

Following [8], we define a set of points in $\mathcal{R}^3$ describing the body of interest as the configuration $\mathcal{M}$ of the body. Points in $\mathcal{M}$ are denoted as $\vec{X} = \{X_1, X_2, X_3\} \in \mathcal{M}$ and are called material points, these labels move with the material. Points in $\mathcal{R}^3$ are denoted as $\vec{x} = \{x_1, x_2, x_3\} \in \mathcal{R}^3$ are called the spatial points. The coordinate system for $\mathcal{R}^3$ is referred to as the spatial system or laboratory frame, while the coordinate system for $\mathcal{M}$ is referred to as the material frame. There exists a smooth, invertible, time-dependent mapping $\vec{x} = \xi(\vec{X}, t),\ \xi : \mathcal{M} \to \mathcal{R}^3$ that describes the motion of $\mathcal{M}$.

It is convention that $\xi(\vec{X}, 0) = \vec{X}$, the two coordinate frames coincide at time $t = 0$. Given two nearby points $\vec{X}$ and $\vec{X} + d\vec{X}$, at some later time t we have

$$\vec{x}(\vec{X}, t) - \vec{x}(\vec{X} + d\vec{X}, t) \approx \frac{\partial \vec{x}}{\partial \vec{X}} d\vec{X} = \overline{F}\, d\vec{X}, \tag{11}$$

where $\overline{F}$ is the deformation gradient, with $F_{iA} = \partial x_i / \partial X_A$. In general the deformation consists of a composition of rotation and stretch, this can be expressed as $\overline{F} = \overline{V}\overline{R}$ where $\overline{R}$ is an orthonormal rotation matrix and $\overline{V}^2 = \overline{B} = \overline{F}\overline{F}^T$ is a symmetric positive definite tensor called the left Cauchy–Green deformation tensor. The tensor $\overline{V}$ is called the left stretch tensor. Since $\overline{V}$ is symmetric positive definite it has the decomposition $\overline{V} = \overline{M}\overline{\Lambda}\overline{M}^T$ where $\overline{M}$ is a unitary matrix defining an orthogonal coordinate system and $\overline{\Lambda}$ is a diagonal matrix with three entries λ_1, λ_2, λ_3, the eigenvalues of $\overline{V}$. The values λ_1, λ_2, λ_3 are called the principle stretches and correspond to the amount of stretching along the three orthogonal coordinate axes. The Jacobian, the ratio between deformed volume and reference volume, is given by

$$J = \sqrt{det(\overline{B})} = det(\overline{F}) = \lambda_1\lambda_2\lambda_3. \tag{12}$$

An alternative decomposition of the deformation gradient is $\overline{F} = \overline{R}\overline{U}$ where $\overline{R}$ is again an orthonormal rotation matrix and $\overline{U}^2 = \overline{C} = \overline{F}^T\overline{F}$ is a symmetric positive definite tensor called the right Cauchy–Green deformation tensor and $\overline{U}$ is called the right stretch tensor. The eigenvalues of $\overline{V}$ equal the eigenvalues of $\overline{U}$. In the former case of $d\vec{x} = \overline{V}\overline{R}d\vec{X}$ the line segment $d\vec{X}$ is rotated then stretched, in the latter case of $d\vec{x} = \overline{R}\overline{U}d\vec{X}$ the line segment is stretched then rotated.

The displacement of a material point is defined as

$$\vec{u}\left(\vec{X}, t\right) = \vec{x}\left(\vec{X}, t\right) - \vec{X}. \tag{13}$$

The displacement gradient is

$$\frac{\partial \vec{u}}{\partial \vec{X}} = \overline{F} - \overline{I}. \tag{14}$$

There are numerous strain measures, the Lagrangian finite strain tensor is a measure of how much the right Cauchy–Green deformation tensor differs from $\overline{I}$,

$$\overline{E} = \frac{1}{2}(\overline{C} - \overline{I}). \tag{15}$$

For the PDMS film of interest here, there is significant deformation and the linear elasticity approximation is not adequate. A hyperelastic material is a material in which the Cauchy stress is function of a scalar strain energy density function W, where W is a function of the invariants of the deformation. Here we will employ an isotropic, homogeneous, hyperelastic model called the Mooney–Rivlin constitutive relation. The strain energy density is given in terms of the invariants of the Cauchy–Green deformation tensor,

$$W = a(I_1 - 3) + b(I_2 - 3) + c\left(\frac{1}{I_3^2} - 1\right) + d(I_3 - 1)^2, \tag{16}$$

where $c = \frac{1}{2}a + b,\ d = \frac{a(5\nu-2)+b(11\nu-5)}{2(1-2\nu)}$, a and b are independent phenomenological constants related to the shear moduli through $G = 2(a+b)$, ν is Poisson's ratio, $\{I_1, I_2, I_3\}$ are the invariants of the Cauchy–Green deformation tensor and can be represented in terms of the principal stretches $(\lambda_1, \lambda_2, \lambda_3)$ as: $I_1 = \lambda_1^2 + \lambda_2^2 + \lambda_3^2, I_2 = \lambda_1^2\lambda_2^2 + \lambda_2^2\lambda_3^2 + \lambda_1^2\lambda_3^2$ and $I_3 = \lambda_1^2\lambda_2^2\lambda_3^2$. The Cauchy stress $\overline{T}_c$ can be expressed in terms of the Piola–Kirchoff stress $\overline{S}$, and the Piola–Kirchoff stress can be expressed in terms of the strain energy W,

$$\overline{T}_c = \frac{1}{J}\overline{F}\overline{S}\overline{F}^T,$$
$$\overline{E} = \frac{1}{2}(\overline{F}^T\overline{F} - \overline{I}),$$
$$\overline{S} = \frac{\partial W}{\partial \overline{E}}.$$

A straightforward but tedious calculation results in the formula for the Cauchy stress tensor as a function of the deformation

$$\overline{T}_c = \frac{1}{J}\left[2(a + bI_1)\overline{B} - 2b\overline{B}^2 + 4\left(-c\frac{1}{I_3^2} + dI_3(I_3 - 1)\right)\overline{I}\right]. \tag{17}$$

2.2. Variational statements

The variational statements are derived by multiplying the partial differential equations above by suitable testing functions, integrating over the domain, and invoking integration by parts formulas. Due to different compatibility requirements, different testing functions will be used for the different partial differential equations.

For Cauchy's equation of motion we require $\vec{u} \in (H(Grad))^3$, the displacement is a fully continuous vector field. The variational form of (9) is constructed by multiplying by a test vector $\vec{U} \in (H(Grad))^3$ and integrating over the entire domain Ω,

$$\int_\Omega \rho \frac{\partial^2 \vec{u}}{\partial t^2} \cdot \vec{U}\, dv = \int_\Omega (\vec{\nabla} \cdot \overline{T}) \cdot \vec{U}\, dv + \int_\Omega \rho \vec{b} \cdot \vec{U}\, dv. \tag{18}$$

If the test vector $\vec{U}$ is considered to have units of distance, then each term in the above equation has units of work, and hence this variational method is often referred to as the Method of Virtual Work. Integration by parts is employed to yield

$$\int_\Omega \rho \frac{\partial^2 \vec{u}}{\partial t^2} \cdot \vec{U}\, dv = \int_\Omega \overline{T} : \left(\vec{\nabla} \otimes \vec{U}\right) dv + \int_\Omega \rho \vec{b} \cdot \vec{U}\, dv + \int_\Gamma (\overline{T}\hat{n}) \cdot \vec{U}\, da, \tag{19}$$

where the notation $\overline{A} : \overline{B}$ represents the tensor dot product, e.g. $\overline{A} : \overline{B} = A_{ij}B_{ij}$, the symbol $\otimes$ denotes the vector outer product, and Γ is the boundary of the domain Ω with an outward unit normal of $\hat{n}$.

In Poisson's equation we require $\Phi_E \in H(Grad)$, the potential is a continuous scalar field. The variational form of (5) is standard, the equation is multiplied by a scalar test function $X \in H(Grad)$ and integrated over the domain Ω to yield

$$\int_\Omega (\vec{\nabla} \cdot \sigma\vec{\nabla}\Phi_E) X\, dv = 0.$$

Green's first scalar identity is used to obtain

$$\int_\Omega \sigma\vec{\nabla}\Phi_E \cdot \vec{\nabla}X\, dv = \oint_\Gamma \hat{n} \cdot \sigma\vec{\nabla}\Phi_E X\, da, \tag{20}$$

which is to be satisfied for all test functions X.

Ampere's law requires $\vec{E}_{ind} \in H(Curl)$, the electric field must have a finite curl. Across material interfaces the tangential component of the $\vec{E}_{ind}$ is continuous, but the normal component may be discontinuous. The variational form is obtained by multiplying Ampere's law (6) by a test function $\vec{W} \in H(Curl)$ and integrating over the three-dimensional problem domain Ω to obtain the variational form

$$\int_\Omega \sigma\vec{E}_{ind} \cdot \vec{W}\, dv = \int_\Omega \vec{\nabla} \times \frac{1}{\mu}\vec{B} \cdot \vec{W}\, dv + \int_\Omega \sigma\vec{\nabla}\Phi_E \cdot \vec{W}\, dv. \tag{21}$$

Now integration by parts is used on (21) and with the Gauss divergence theorem the result is

$$\int_\Omega \sigma\vec{E}_{ind} \cdot \vec{W}\, dv = -\int_\Omega \frac{1}{\mu}\vec{B} \cdot \vec{\nabla} \times \vec{W}\, dv + \int_\Omega \sigma\vec{\nabla}\Phi_E \cdot \vec{W}\, dv + \oint_\Gamma \hat{n} \times \frac{1}{\mu}\vec{B} \cdot \vec{W}\, da. \tag{22}$$

The resulting surface integral term has units of electrical current and will become important when we discuss boundary conditions; but for the sake of clarity, we will omit this term for the remaining derivation.

The magnetic flux density must satisfy $\vec{B} \in H(Div)$, $\vec{B}$ must have a finite divergence, and across material interfaces the normal component must be continuous, but the tangential component may be discontinuous. The variational form of

Faraday's law is obtained by multiplying by a test function $\vec{V} \in H(Div)$ and integrating over the three-dimensional problem domain Ω to yield

$$\int_\Omega \frac{\partial \vec{B}}{\partial t} \cdot \vec{V}\, dv = -\int_\Omega \vec{\nabla} \times \vec{E}_{ind} \cdot \vec{V}\, dv. \tag{23}$$

No integration by parts is required for this equation.

The natural and essential boundary conditions for (19) are

$$\begin{aligned} &\text{Natural} \quad \overline{T}\hat{n} = 0, \\ &\text{Essential} \quad \vec{u} = 0. \end{aligned} \tag{24}$$

In general, the inhomogeneous boundary conditions require vector-valued functions $\vec{t}_b$ and $\vec{u}_b$ such that

$$\begin{aligned} &\overline{T}\hat{n} = \vec{t}_b \quad \text{on } \Gamma_t, \\ &\vec{u} = \vec{u}_b \quad \text{on } \Gamma_u, \end{aligned}$$

where Γ_u and Γ_t are the portion of the boundary where displacement and traction are prescribed respectively, note that $\Gamma_u \cup \Gamma_t = \Gamma$.

The natural and essential boundary conditions for (20) are

$$\begin{aligned} &\text{Natural} \quad \hat{n} \cdot \sigma \vec{\nabla} \Phi_E = 0, \\ &\text{Essential} \quad \Phi_E = 0. \end{aligned} \tag{25}$$

In other words, the normal component of the conduction current density $\sigma \vec{\nabla} \Phi_E$ is the natural boundary condition while the surface scalar potential (or voltage) Φ_E is the essential boundary condition. In general, the inhomogeneous versions of these two boundary conditions require scalar valued functions g_N and g_D such that

$$\begin{aligned} &\hat{n} \cdot \sigma \vec{\nabla} \Phi_E = g_N \quad \text{on} \quad \Gamma_N, \\ &\Phi_E = g_D \quad \text{on} \quad \Gamma_D, \end{aligned}$$

where Γ_N and Γ_D are portion of the boundary where current density and scalar potential are prescribed respectively note that $\Gamma_N \cup \Gamma_D = \Gamma$.

The natural and essential boundary conditions for (22) are

$$\begin{aligned} &\text{Natural} \quad \hat{n} \times \frac{1}{\mu}\vec{B} = 0, \\ &\text{Essential} \quad \hat{n} \times \vec{E}_{ind} = 0. \end{aligned} \tag{26}$$

In general, the inhomogeneous versions of these two boundary conditions require vector-valued functions $\vec{g}_N$ and $\vec{g}_D$ such that

$$\begin{aligned} &\hat{n} \times \frac{1}{\mu}\vec{B} = \vec{g}_N \quad \text{on } \Gamma_N, \\ &\hat{n} \times \vec{E} = \vec{g}_D \quad \text{on } \Gamma_D. \end{aligned}$$

2.3. Finite element basis functions

The variation forms above employ four different function spaces, $\vec{U} \subset (H(Grad))^3$ for the displacement, $X \subset H(Grad)$ for the scalar potential, $\vec{W} \subset H(Curl)$ for the electric field, and $\vec{V} \subset H(Div)$ for the magnetic flux density. We will use different finite element basis functions for each of these spaces. The basis functions are defined on a computational mesh, for our application the mesh is a conforming unstructured mesh of hexahedral elements. Each basis function is constructed to preserve the characteristic of the quantities they are used to represent.

The simplest basis function that is $X \subset H(Grad)$ conforming is a collection of piecewise linear nodal interpolatory basis functions. This can be represented by Ψ_I for $I = 1 \ldots N$ for each mesh node I where N is the total number of nodes. This can be interpolated on nodes meaning that if $\vec{x}_J$ is the position of node J where $J = 1 \ldots N$, then

$$\Psi_I(\vec{x}_J) = \delta_{IJ}, \tag{27}$$

The electric scalar potential Φ_E at a position of $\vec{x}$ is then given by the basis function expansion

$$\Phi_E(\vec{x}) = \sum_{I=1}^{N} \phi_I \Psi_I(\vec{x}), \tag{28}$$

where ϕ_I is the value of the potential at mesh node I.

The functions $\vec{U} \subset (H(Grad))^3$ are discretized using the basis functions Ψ_I for each component of the vector. This can be represented as $\vec{\Psi}_I^k$ where $\vec{\Psi}_I^1 = \hat{x}^1 \Psi_I$, $\vec{\Psi}_I^2 = \hat{x}^2 \Psi_I$, and $\vec{\Psi}_I^3 = \hat{x}^3 \Psi_I$ are vector-valued basis functions in the x^1, x^2, and x^3 directions. This can be interpolated on nodes meaning that if $\vec{x}_J = \hat{x}^i x_J^i$ where $i = 1 \ldots 3$ is the position of node $J = 1 \ldots N$, then

$$\vec{\Psi}_I^i x_J^j = \delta_{JK} \delta_{ij}, \tag{29}$$

where $j = 1 \ldots 3$. The basis function expansion of the displacement $\vec{u}$ at a position of $\vec{x}$ is given by

$$\vec{u}(\vec{x}) = \sum_{I=1}^{N} u_I^i \vec{\Psi}_I^i(\vec{x}) \tag{30}$$

respectively. The coefficient u_I^i is the value of the ith component of the displacement at mesh node I. It is more notationally convenient to eliminate the superscript i and instead allow the index K to run from $K = 1 \ldots 3N$, with $u_K = u_I^i,\ i = K \bmod 3,\ I = (K-1)/3 + 1$.

There has been much analysis of various basis functions for the spaces $H(Curl)$ and $H(Div)$. We do not provide any original analysis here, rather we will simply review the key properties of the so-called "edge" $H(Curl)$-conforming basis functions and "face" $H(Div)$-conforming basis functions. The edge basis functions $\vec{W} \subset (H(Curl))$ are piecewise linear basis functions defined on the computational mesh. This basis functions can be represented as $\vec{\Theta}_A$ for $A = 1 \ldots M$, where M is the number of mesh edges, these functions interpolate on edges, meaning that if $\hat{t}_B$ is the edge vector of edge $B = 1 \ldots M$, then

$$\int_L \vec{\Theta}_A \cdot \hat{t}_B \, dl = \delta_{AB}, \tag{31}$$

where the line integral is over mesh edge A. The electric field at position $\vec{x}$ is given by the basis function expansion

$$\vec{E}_{inc}(\vec{x}) = \sum_{A=1}^{M} e_A \vec{\Theta}_A(\vec{x}), \tag{32}$$

where e_A is the induced voltage along edge A. It is convenient to implement the edge basis functions on a reference hexahedron and then transform to the actual element. Eq. (31) implies that the appropriate transformation for the basis functions is

$$\vec{\Theta}_A = \overline{F}^{-T} \vec{\Theta}'_A, \tag{33}$$

where $\overline{F}$ is the deformation tensor defined in the discussion of the Mooney–Rivlin material model, and prime denotes the reference basis function. This transformation preserves the continuity of the tangential component of the field across element material interfaces, but allows for the normal component to be discontinuous, which is the correct physical continuity of electric fields.

The face basis functions $\vec{V} \subset (H(Div))$ are also piecewise linear basis functions defined on the computational mesh. This basis functions can be represented as $\vec{\Lambda}_C$ for $C = 1 \ldots F$, where F is the number of mesh faces, interpolate on faces, these basis functions meaning that if $\hat{n}_D$ is an face normal vector $D = 1 \ldots F$, then

$$\int_A \vec{\Lambda}_C \cdot \hat{n}_D da = \delta_{CD}, \tag{34}$$

where the surface integral is over mesh face C. The magnetic flux density at position $\vec{x}$ is given by the basis function expansion

$$\vec{B}(\vec{x}) = \sum_{D=1}^{F} b_C \vec{\Lambda}_C(\vec{x}), \tag{35}$$

where b_C is the net flux through face C. It is convenient to implement the face basis functions on a reference hexahedron and then transform to the actual element. Eq. (34) implies that the appropriate transformation for the basis functions is

$$\vec{\Lambda}_C = \frac{1}{J} \overline{F}^T \vec{\Lambda}'_C, \tag{36}$$

where $\overline{F}$ is the deformation tensor, J is the element Jacobian, and prime denotes the reference basis function. This transformation preserves the continuity of the normal component of the field across element material interfaces, but allows for the tangential component to be discontinuous, which is the correct physical continuity of magnetic flux.

Another key property of the node, edge and face basis functions is the inclusion relations,

$$\vec{\nabla} X \in \vec{W}, \tag{37}$$

$$\vec{\nabla} \times \vec{W} \in \vec{V} \tag{38}$$

which is simple version of the De-Rham complex [21]. These inclusion relations allow for discrete versions of the vector identities $\vec{\nabla} \times \vec{\nabla} f = 0$ and $\vec{\nabla} \cdot \vec{\nabla} \times g = 0$ to be satisfied exactly.

Using the basis functions described above the discrete variation forms can be written as

$$\mathbf{M}\frac{\partial^2}{\partial t^2}\mathbf{u} + \mathbf{K}(\mathbf{u}) = \mathbf{f}, \tag{39}$$

$$\mathbf{S}\boldsymbol{\phi} = \mathbf{g}, \tag{40}$$

$$\mathbf{M}^W\mathbf{e} = (\mathbf{D}^{WV})^T\mathbf{b} + \mathbf{D}^{XW}\boldsymbol{\phi} - \mathbf{r}, \tag{41}$$

$$\mathbf{M}^V\frac{\partial}{\partial t}\mathbf{b} = \mathbf{D}^{WV}\mathbf{e}, \tag{42}$$

where $\mathbf{u}$, $\boldsymbol{\phi}$, $\mathbf{e}$, and $\mathbf{b}$ are the arrays of coefficients for the basis function expansion of the displacement, the electrostatic potential, the electric field, and the magnetic field, respectively. The matrices are given by

$$M_{KL} = \int_\Omega \rho\vec{\Psi}_K \cdot \vec{\Psi}_L \, d\Omega, \tag{43}$$

$$K_{KL}(\mathbf{u}) = \int_\Omega \overline{T}_K(\mathbf{u}) : \vec{\nabla}\vec{\Psi}_L \, d\Omega, \tag{44}$$

$$S_{IJ} = \int_\Omega \sigma\vec{\nabla}\Psi_I \cdot \vec{\nabla}\Psi_J \, d\Omega, \tag{45}$$

$$M^W_{AB} = \int_\Omega \rho\vec{\Theta}_A \cdot \vec{\Theta}_B \, d\Omega, \tag{46}$$

$$M^V_{CD} = \int_\Omega \vec{\Lambda}_C \cdot \vec{\Lambda}_D \, d\Omega, \tag{47}$$

$$D^{WV}_{AC} = \int_\Omega \frac{1}{\mu}\vec{\nabla} \times \vec{\Theta}_A \cdot \vec{\Lambda}_C \, d\Omega, \tag{48}$$

$$D^{XW}_{IA} = \int_\Omega \vec{\nabla}\Psi_I \cdot \vec{\Theta}_A \, d\Omega. \tag{49}$$

The various basis functions, quadratures, and mappings for all of the above matrices have been implemented in the FEMSTER library [22,23]. The matrices are computed using standard finite element procedures, i.e. each subscript pair (KL, IJ, AB, CD, AC and IA) interaction is computed in a reference element using Gaussian quadrature, this result is transformed to the actual element, and the final result is accumulated in a sparse matrix data structure. Note that in the material stiffness matrix $\mathbf{K}$ the stress tensor is a complicated nonlinear function of both the displacement $\mathbf{u}$ and the magnetic fields, and for simplicity the stress is assumed constant over each element. Also note that Eq. (42) can be simplified using the inclusion relations, the matrix $\mathbf{D}^{WV}$ can be written as $\mathbf{D}^{WV} = \mathbf{M}^V\mathbf{K}^{WV}$, where $\mathbf{K}^{WV}$ is an edge-face incidence matrix. Therefore (42) can be written as

$$\frac{\partial}{\partial t}\mathbf{b} = \mathbf{K}^{WV}\mathbf{e}, \tag{50}$$

it is an explicit relation. As another side note, the divergence constraints (1) and (2) can be expressed as

$$(\mathbf{D}^{XW})^T\mathbf{e} = 0, \tag{51}$$

$$\mathbf{K}^{WV}\mathbf{b} = 0. \tag{52}$$

The matrix $\mathbf{D}^{XW}$ can be decomposed as $\mathbf{D}^{XW} = \mathbf{M}^W\mathbf{K}^{XW}$, where $\mathbf{K}^{XW}$ is a node-edge incidence matrix. From the topological identity $\mathbf{K}^{WV}\mathbf{K}^{XW} = 0$, it is clear that the discrete divergence conditions (51) and (52) are satisfied automatically, for any mesh, without the need to introduce Lagrange multipliers or a penalty method. In words, at every node in the mesh the edge-based electric fields sum to zero, and at every element in the mesh all face-based magnetic fluxes sum to zero. This is one advantage of using the edge and face basis functions for finite element electromagnetics.

The arrays $\mathbf{f}$, $\mathbf{g}$, and $\mathbf{r}$ are the coefficients for the independent source terms. The array $\mathbf{f}$ involves a body force such as gravity and a surface traction, the array $\mathbf{g}$ involves current injected into the problem domain, and the array $\mathbf{r}$ involves a surface current density,

$$f_K = \int_\Omega \rho\vec{b} \cdot \vec{\Psi}_K \, d\Omega + \int_\Gamma (\overline{T}\hat{n}) \cdot \vec{\Psi}_K \, d\Gamma, \tag{53}$$

$$g_I = \int_\Gamma (\hat{n} \cdot \sigma\vec{\nabla}\Phi)\Psi_I \, da, \tag{54}$$

$$r_A = \int_\Gamma \hat{n} \times \frac{1}{\mu}\vec{B} \cdot \vec{\Theta}_A \, da. \tag{55}$$

2.4. Time integration

The elastic equations and the Maxwell equations will be integrated in time implicitly, but in an operator split manner. When updating the displacement the electromagnetic fields are held constant, and when updating the electromagnetic fields

the displacement is held constant. Operator splitting is a well known approximation often used in multi-physics simulations, the error can be shown to be of first order accurate with respect to the time step Δt.

In the semi-discrete equation of motion (39) the displacement coefficients $\mathbf{u}$ are continuous functions of time. Time integration is achieved by using finite difference methods in which $\mathbf{u}$ is known at discrete instants. Let superscript n denote the discrete-time index, with $t^{n+1} - t^n = \Delta t$. Let $\mathbf{a}$ and $\mathbf{v}$ denote $\frac{\partial^2}{\partial t^2}\mathbf{u}$ and $\frac{\partial}{\partial t}\mathbf{u}$, respectively. The Newmark family of time integration methods is given by

$$\mathbf{M}\mathbf{a}^{n+1} + \mathbf{K}(\mathbf{u}^{n+1}) = \mathbf{F}^{n+1}, \tag{56}$$

$$\mathbf{v}^{n+1} = \mathbf{v}^n + \Delta t[(1-\gamma)\mathbf{a}^n + \gamma\mathbf{a}^{n+1}], \tag{57}$$

$$\mathbf{u}^{n+1} = \mathbf{u}^n + \Delta t\mathbf{v}^n + \Delta t^2\left[\left(\frac{1}{2} - \beta\right)\mathbf{a}^n + \beta\mathbf{a}^{n+1}\right], \tag{58}$$

where γ and β are arbitrary parameters in the intervals $[0,1]$ and $\left[0,\frac{1}{2}\right]$, respectively. For linear elasticity it is common to solve (56) for the acceleration $\mathbf{a}^{n+1}$, this acceleration is used in (57) to update the velocity $\mathbf{v}^{n+1}$, and the velocity is used in (58) to update the displacement $\mathbf{u}^{n+1}$. For the linear case the accuracy and stability of the method can be analyzed. The special values of $\beta = 1/4$ and $\gamma = 1/2$ give the trapezoidal rule, or average acceleration method, which is second-order accurate and unconditionally stable. However, since the stress $\overline{T}$ is a nonlinear function of $\mathbf{u}$ for the Mooney–Rivlin model, it is necessary to express $\mathbf{a}^{n+1}$ in terms of $\mathbf{u}^{n+1}$,

$$\mathbf{a}^{n+1} = \frac{1}{\Delta t^2\beta}\mathbf{u}^{n+1} - \frac{1}{\Delta t^2\beta}\mathbf{u}^n - \frac{1}{\Delta t\beta}\mathbf{v}^n - \frac{1-2\beta}{2\beta}\mathbf{a}^n \tag{59}$$

and then this is used in (56) to give

$$\frac{1}{\Delta t^2\beta}\mathbf{M}\mathbf{u}^{n+1} + \mathbf{K}(\mathbf{u}^{n+1}) = \mathbf{F}^{n+1} + \mathbf{M}\frac{1}{\Delta t^2\beta}\mathbf{u}^n + \mathbf{M}\frac{1}{\Delta t\beta}\mathbf{v}^n + \mathbf{M}\frac{1-2\beta}{2\beta}\mathbf{a}^n \tag{60}$$

giving a nonlinear equation for $\mathbf{u}^{n+1}$ in terms of known quantities.

For the magnetic film application it is desirable to add a controlled amount of dissipation into the time integration algorithm in order to damp out high-frequency waves and to more rapidly converge to a steady-state solution. The Hilber–Hughes–Taylor integrator modifies (56) by adding an additional parameter α,

$$\mathbf{M}\mathbf{a}^{n+1} + (1+\alpha)\mathbf{K}(\mathbf{u}^{n+1}) = \alpha\mathbf{K}(\mathbf{u}^n) + \mathbf{F}^{n+1}, \tag{61}$$

where α is an independent parameter. This results in the final form of the full-discrete equation of motion,

$$\frac{1}{\Delta t^2\beta}\mathbf{M}\mathbf{u}^{n+1} + (1+\alpha)\mathbf{K}(\mathbf{u}^{n+1}) = \alpha\mathbf{K}(\mathbf{u}^n) + \mathbf{F}^{n+1} + \mathbf{M}\frac{1}{\Delta t^2\beta}\mathbf{u}^n + \mathbf{M}\frac{1}{\Delta\beta}\mathbf{v}^n + \mathbf{M}\frac{1-2\beta}{2\beta}\mathbf{a}^n. \tag{62}$$

The same Eqs. (57) and (58) are used to integrate acceleration and velocity. The HHT integration method will be unconditionally stable and second-order accurate provided $\alpha \in [-1/3, 0]$ and

$$\gamma = \frac{1-2\alpha}{2}, \tag{63}$$

$$\beta = \frac{(1-\alpha)^2}{4}. \tag{64}$$

To form a discrete-time set of equations for the electromagnetic coefficients $\mathbf{e}$, $\mathbf{b}$ and $\boldsymbol{\phi}$ are known at discrete time intervals denoted by the subscript integer n. The fully discrete form of Poisson's equation and Ampere's law become

$$\mathbf{S}^X\boldsymbol{\phi}^{n+1} = \mathbf{g}^{n+1}, \tag{65}$$

$$\mathbf{M}^W\mathbf{e}^{n+1} = (\mathbf{D}^{WV})^T\mathbf{b}^{n+1} + \mathbf{D}^{XW}\boldsymbol{\phi}^{n+1} - \mathbf{r}^{n+1}. \tag{66}$$

A generalized trapezoidal approximation is used for the time derivative of the magnetic field such that

$$\mathbf{b}^{n+1} = \mathbf{b}^n + (1-\omega)\Delta t\left.\frac{\partial\mathbf{b}}{\partial t}\right|^n + \omega\Delta t\left.\frac{\partial\mathbf{b}}{\partial t}\right|^{n+1}. \tag{67}$$

The averaging parameter ω determines the nature of the numerical time integration such that

$$\omega = \begin{cases} 0, & \text{Explicit, 1st Order Accurate Forward Euler,} \\ 1/2, & \text{Implicit, 2nd Order Accurate Crank Nicolson,} \\ 1, & \text{Implicit, 1st Order Accurate Backward Euler.} \end{cases}$$

Applying this discretization to the semi-discrete Faraday's law (50), gives

$$\mathbf{b}^{n+1} = \mathbf{b}^n - \Delta t((1-\omega)\mathbf{K}^{WV}\mathbf{e}^n + \omega\mathbf{K}^{WV}\mathbf{e}^{n+1}). \tag{68}$$

An intermediate variable is introduced, $\tilde{\mathbf{b}}$, defined as

$$\tilde{\mathbf{b}}^n = \mathbf{b}^n - (1-\omega)\Delta t \mathbf{K}^{WV}\mathbf{e}^n. \tag{69}$$

Combining (69), (68), and (66) yields the final update equation for $\mathbf{e}^{n+1}$,

$$(\mathbf{M}^W + \omega\Delta t\mathbf{K}^{WV})\mathbf{e}^{n+1} = (\mathbf{D}^{WV})^T\tilde{\mathbf{b}}^n + \mathbf{D}^{XW}\boldsymbol{\phi}^{n+1}. \tag{70}$$

2.5. Mesh relaxation

The above finite element equations for the electromagnetics are valid in the material frame, meaning the computational mesh is fixed to the material and moves with the material. This is ideal for coupling with the equations of finite element elasticity since these equations are also cast in the material frame. However a key difference between the electromagnetics and the elasticity is that magnetic fields exist in the vacuum surrounding the magnetic film, and a region of vacuum surrounding the film must be included in the calculation. The computational mesh is fixed to the film and hence moves with the film, however if the mesh in the vacuum region does not somehow also move, the mesh can become severely distorted and eventually become unacceptable. To remedy this the computational mesh of the vacuum region is allowed to relax. Numerous algorithms exist for mesh relaxation, the method used here is equipotential relaxation which essentially moves each mesh node to the mean value of all surrounding nodes, this can be shown to be a solution to Poisson's equation for the node coordinates. The important concept is that, as the mesh in the vacuum region is adjusted, the magnetic field must be interpolated from the old mesh to the new mesh in a manner that preserves the properties of the field. This interpolation is often referred to as advection, because it is identical to the advection operator $\nabla \times \vec{v} \times \vec{B}$ that appears in the Eulerian solution of magnetic problems with motion. However in the case of mesh relaxation, the velocity $\vec{v} = \Delta\vec{x}/\Delta t$ is not a physical velocity, rather it is just the velocity of the mesh as it is relaxing. It is known that naive numerical methods for the magnetic advection operator result in non-physical oscillations of the fields (reminiscent of Gibb's or Runge's phenomena) hence sophisticated upwind methods with flux limiting must be used. In addition, the advection is complicated by the fact that the magnetic field must remain divergence free. A detailed derivation of a divergence-preserving flux-limited advection algorithm is presented in [10].

2.6. Complete finite element solution process

Here we provide a high-level summary of the finite element solution process for the fully-coupled magnetoelastic equations. The solution sequence is

Step 1. Compute the Maxwell stress tensor (8) using magnetic fields at time t^n.
Step 2. Update the displacement $\mathbf{u}^{n+1}$ using Eq. (62). During this step the Maxwell stress is constant, but the Cauchy stress is given by the hyperelastic Mooney–Rivlin model (17), hence (62) is a nonlinear system of equations. This system of equations is solved using Newtons's method, with a multigrid preconditioner [24,25].
Step 3. Update the velocity (57) and the acceleration (58) and store these values for the next displacement calculation.
Step 4. Update Poisson's equation (65) for the electrostatic potential. The boundary conditions on Φ_E are chosen to drive a current into a coil, generating a dipole-like external magnetic field. This is a linear implicit equation and is s solved using a the same multigrid preconditioner as in Step 2.
Step 5. Update the electric field using (66). This is a linear implicit equation and is solved using a different multigrid preconditioner specifically developed for edge-based discretization of curl–curl equations [26].
Step 6. Update the magnetic field using (50), this is an explicit equation.
Step 7. In the vacuum region, if there has been significant motion of the mesh, relax the mesh and interpolate the magnetic coefficients $\mathbf{b}^{n+1}$ onto the new mesh. No other electromagnetic variables needs to be interpolated as they will be computed "from scratch" during the next update.

This completes one cycle of the magnetoelastic solution process. The process is repeated using a constant time step Δt. The time integration is unconditionally stable, hence the time step is chosen based on accuracy requirements.

3. Analytical model

The above finite element formulation of the magnetoelastic equations is quite general, it can be applied to arbitrary three-dimensional geometries, the applied magnetic field is arbitrary, and the approach can be used to investigate fast transients, or sinusoidal response, or steady-state response. In order to test the finite element formulation it is necessary to construct a simple problem that has an analytical solution. In this section we review the analytical solution to a thin circular magnetoelastic membrane in an external magnetic field. The derivation of this solution can be found [11].

The starting point is the equation of magnetoelastic equilibrium. The geometry is symmetric and the solution is one-dimensional, i.e. the membrane height as a function of radius. It is assumed that the magnetization of the membrane itself

is weak, i.e. the self-field is neglected. The membrane approximation is used, the aspect ratio between film thickness and film radius is small and only the leading oder term in the asymptotic expansion is used. In the membrane approximation there is no resistance to bending. The Mooney–Rivlin model for hyperelasticity is used for the stress as a function of displacement. And finally the external magnetic field is given by an ideal dipole field. This leads to a set of coupled differential equations that is solved numerically using a shooting method,

$$\lambda = u/r, \quad \kappa = \sqrt{u'^2 + z'^2}, \quad \cos\theta = u'/\kappa,$$

$$\kappa' = (r\tilde{w}_{\kappa\kappa})^{-1}\left[\tilde{w}_\lambda \cos\theta - \tilde{w}_\kappa - \tilde{w}_{\lambda\kappa}(\kappa\cos\theta - u/r) + r\frac{H}{l^6}\left(4\frac{(h-z)^3}{l^6}\sin\theta + \left[1 + 4\frac{(h-z)^2}{l^6}\right]u\cos\theta\right)\right],$$

$$\theta' = (r\tilde{w}_\kappa)^{-1}\left[-\tilde{w}_\lambda \sin\theta + r\frac{H}{l^6}\left(4\frac{(h-z)^3}{l^6}\cos\theta + \left[1 + 4\frac{(h-z)^2}{l^6}\right]u\sin\theta\right)\right],$$

where $r \in [0, r_0]$ is the radius from the axis of symmetry of a material point in the reference configuration; $\lambda(r)$ and $\kappa(r)$ are the azimuthal and radial principal stretches; $u(r)$ and $z(r)$ are the radial and axial coordinates of a material point in the deformed configuration; $\phi(r)$ is an angle defined in Fig. 1; h is the assigned distance between the dipole and the mid-plane of the undeformed film; l is the distance from the dipole to a deformed material point ($l^2 = u^2 + (h-z)^2$; $\tilde{w} = t_f W$; $H = 3D^2\mu_0\chi t_f$; W is the conventional strain energy function dependent on the principal stretches; D is the dipole strength; μ_0 is the free-space permeability; χ is the films magnetic susceptibility; t_f is the film thickness. Refer to Fig. 1 for a geometric representation. Note that the notation $(\cdot)' = d(\cdot)/dr$ and Greek or Latin subscripts are used to denote partial derivatives.

We can solve for $\tilde{w}$ with the use of the Mooney–Rivlin strain energy function (Eq. (16)), incompressibility ($\lambda_1\lambda_2\lambda_3 = 1$) and the relation between W and $\tilde{w}$ arriving at:

$$\tilde{w}(\lambda,\kappa) = \frac{t_f G}{2}\left[\delta(\lambda^2 + \kappa^2 + \lambda^{-2}\kappa^{-2} - 3) + (1-\delta)(\lambda^{-2} + \kappa^{-2} + \lambda^2\kappa^2 - 3)\right]. \tag{71}$$

The above system is solved using a shooting method.

The goal is to compare full 3D finite thickness finite element simulations to this analytical model. It is seen that the only place the film thickness appears in the analytical equilibrium equations is in $H = 3D^2\mu_0\chi t_f$ and $G^* = t_f G$. If the thickness is parameterized by a constant ε, as in $t_f^{new} = t_f^{old}$, we can adjust the values of the dipole strength (D) and shear modulus (G) as follows to maintain an equivalent comparison,

$$D_{new} = D_{old}\sqrt{\frac{1}{\varepsilon}}, \tag{72}$$

$$G_{new} = G_{old}\frac{1}{\varepsilon}. \tag{73}$$

4. Finite element results

The magnetoelastic film is a thin circular disk of thickness ϵ and radius $r_0 = 0.317$ cm is centered in the $x-y$ plane, with displacement in the z direction. The thickness will be varied using values $t_f = (140, 70, 35, 17.5)$ μm in order to investigate

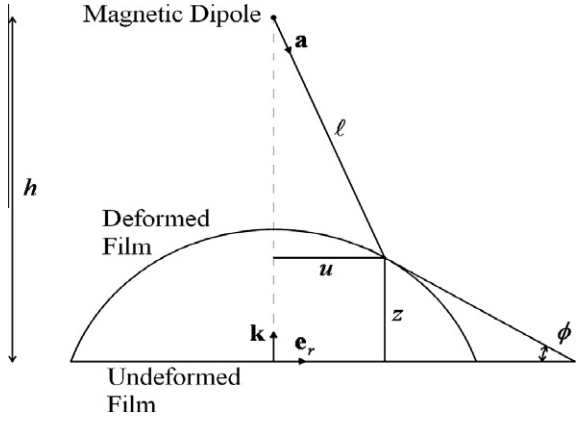

Fig. 1. Geometry for the membrane approximation.

deformation vs thickness. A small steel ring, with a fixed electric current, is used to create a magnetic field similar to a magnetic dipole. The ring is located a distance h above the membrane. The finite element formulation is inherently three-dimensional, and hence it is possible to simulate deviations from symmetry, but to compare to the analytical membrane approximation symmetry is enforced by appropriate boundary conditions. Only one quarter of the problem is meshed around the axis of symmetry, i.e. the $x \geqslant 0$ and $y \geqslant 0$ quadrant, and displacement symmetry boundary conditions are imposed on the $x = 0$ and $y = 0$ planes. The geometry for the finite element simulation is illustrated in 1. For the thickness of $t_f =$ (140, 70, 35) μm the film was four elements thick, for the thickness of $t_f = 17.5$ μm the film was two elements thick. The computational mesh consisted of 43,200 elements and 42,048 elements for these two cases. On all mesh boundaries that are not symmetry planes the displacement is constrained to be zero. The displacement on the edge of the film is also constrained. The entire edge of the film is not constrained since this would impose zero slope as well as the desired zero displacement. To get a better comparison to the membrane model, only the nodes on the mid-plane are constrained, this allows for rotation at the edge of the film while maintaining zero displacement of the mid-plane at the edge. The geometry is illustrated in Fig. 2.

Since the current carrying ring used in the finite element simulation does not produce an exact magnetic dipole field, an equivalent dipole strength (D_{eq}) for comparison to the analytical model is needed. Given the magnetic field produced by a given current in the steel ring, an equivalent dipole strength is calculated for each mesh element between $0 \leqslant r \leqslant r_0$ and $h + t_f/2 \leqslant z \leqslant 7h/5$ and the average of the equivalent dipole strengths will be used for comparison. The dipole magnetic field used in the continuum model is:

$$\mathbf{H} = D\frac{3(\mathbf{a}\cdot\mathbf{k})\mathbf{a} - \mathbf{k}}{l^3}, \tag{74}$$

where $\mathbf{a}$ is the unit vector from the dipole to a material point. The equivalent dipole strength is determined by taking the dot product between the right hand side of (74) with the unit vector in z-direction and setting this equal to the z-component of the magnetic field produced by the FEM resulting in:

$$H_{zFEM} = D_{eq}\frac{2(z_c - h)^2 - r_c^2}{l^5}, \tag{75}$$

and when the solving for the equivalent dipole strength:

$$D_{eq} = \frac{l^5 H_{zFEM}}{2(z_c - h)^2 - r_c^2}, \tag{76}$$

where z_c is the height of the center of the element above the mid-pane of the film and r_c is the radial position of the center of the element away from the axis of symmetry. It should be noted that the relationship between the equivalent dipole strength and the current density is linear. Thus once the equivalent dipole strength is calculated for one current density the equiv-

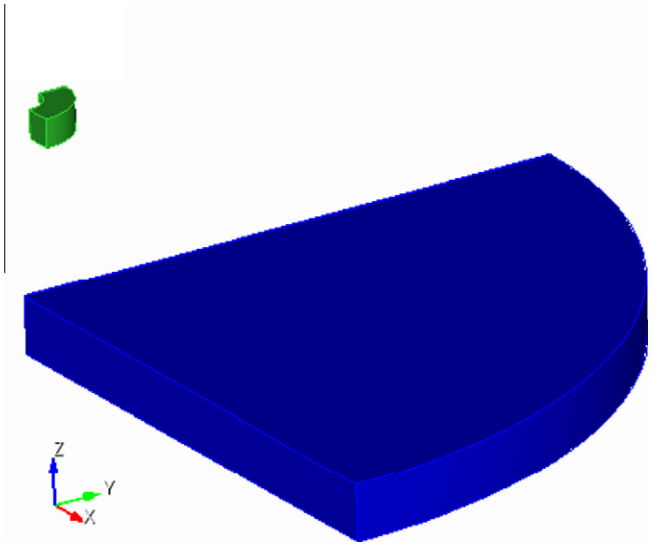

Fig. 2. Illustration of the geometry for the FEM simulations. This illustration is not to scale, the thickness of the membrane and the size of the current carrying ring have been exaggerated for clarity.

alent dipole strength for any other current is known. For comparison of different finite element film thickness it convenient to define $H_{eq} = 3D_{eq}^2 \mu_0 \chi t_f$.

For comparison to the analytical membrane approximation, the finite element simulation is run to steady-state for a specific ring current, which corresponds to a specific effective dipole strength. Then the current is increased to the next effective dipole strength, and the simulation is run to steady-state again. For each simulation, the time step was 10 μs. The number of steps ranged from 15 to 100, more steps were required for the larger effective dipole strength as this gives larger displacement. The process is illustrated in Fig. 3.

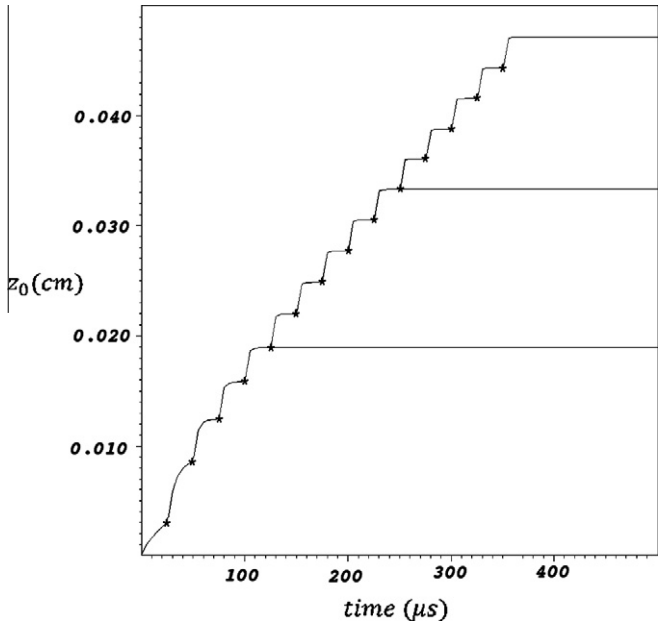

Fig. 3. Center displacement z_0 for increasing dipole strength, increases of 1.55310^{-4} A m^2 at each step.

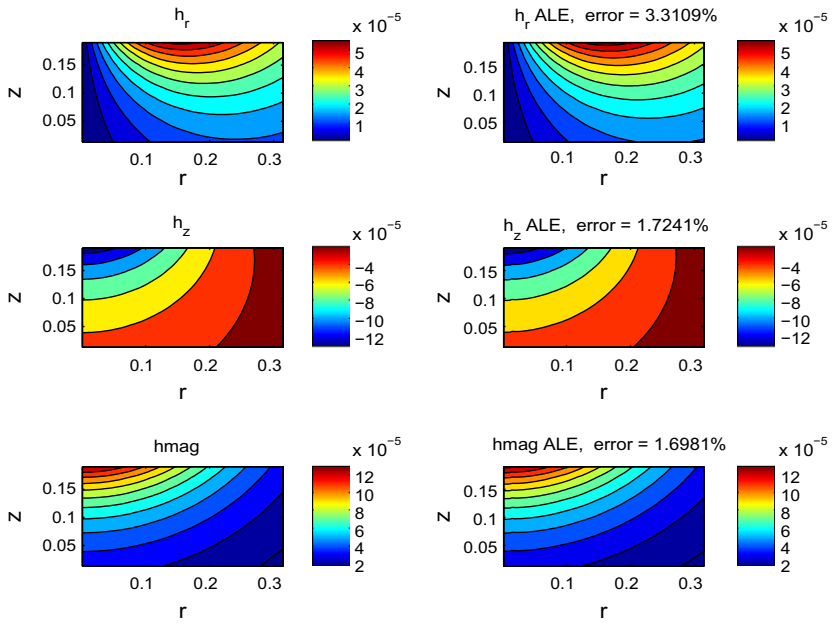

Fig. 4. Magnetic field model. The analytical analysis assumes an idealized infinitesimal magnetic dipole as the source of the magnetic field. The FEM analysis employs a finite current ring. These plots show magnetic field magnitude, just above the membrane, for these two models.

The following results are for a magnetoelastic film with the following properties and dimensions:

Properties	Symbol	Value
Radius of film	r_0	0.317 cm
Dipole height	h	0.5 cm
(Film sheer modulus) × (film thickness)	$Gt_f = G^*$	1750 N/m
Mooney–Rivlin tuning parameter	δ	0.9
Film magnetic susceptibility	χ	2.5
Film thickness	t_f	17.5 – 140 μm
Dipole strengths	D	$0 - .0056\,A^2$ m

Fig. 4 compares the magnetic field produced by the dipole to that of the finite steel ring used in the finite element model. The error shown on the figure is the average error over the elements used to calculate the equivalent dipole strength. These results show that the dipole approximation used in the analytical model is reasonable for this particular geometry, with a maximum error of around 3.3%.

The results of the finite element simulation are shown in Fig. 5. These figures show the final deformation for given effective dipole strengths. A key observation is that the computational mesh in the air moves along with the membrane, this is the mesh relaxation process described in Section 2.5 above. These FEM results are compared to the analytical results in Figs. 6 and 7. In Fig. 6 the displacement is shown versus position for a few discrete values of magnetic dipole strength. In Fig. 7 the displacement at the membrane center is shown versus continuous magnetic dipole strength. The comparison is good,

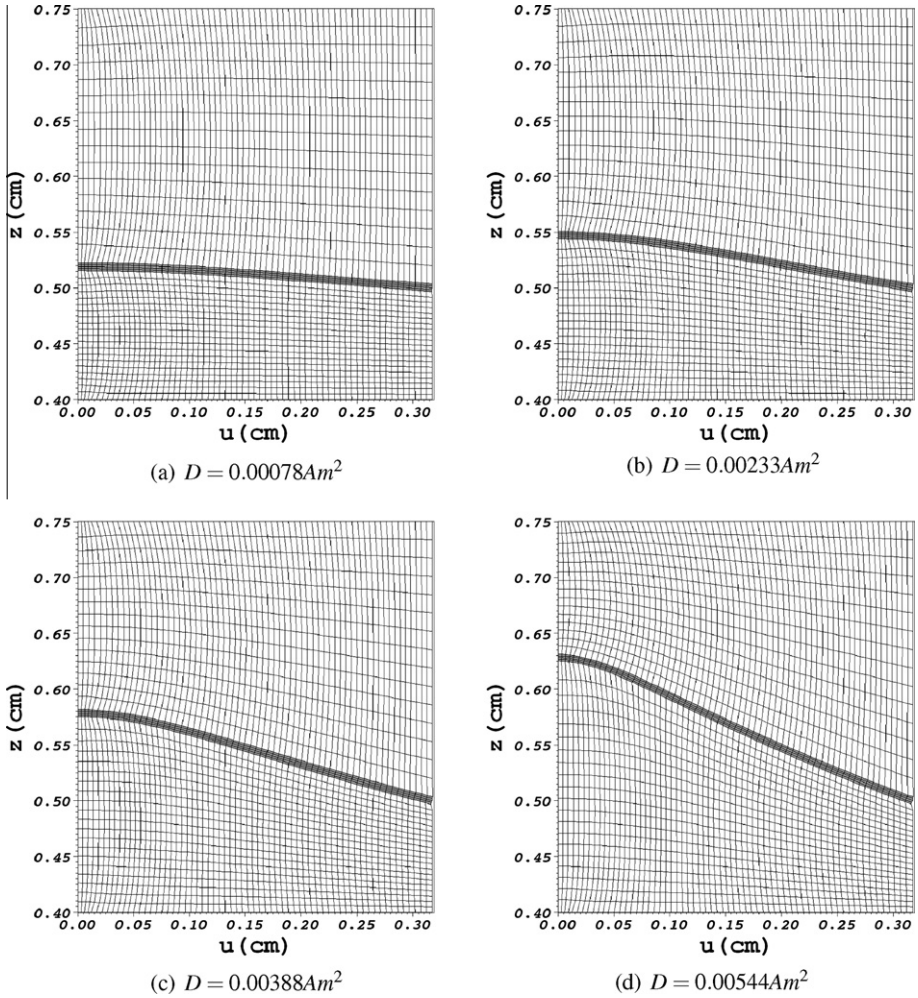

(a) $D = 0.00078 Am^2$ (b) $D = 0.00233 Am^2$

(c) $D = 0.00388 Am^2$ (d) $D = 0.00544 Am^2$

Fig. 5. Displacement for the FEM model.

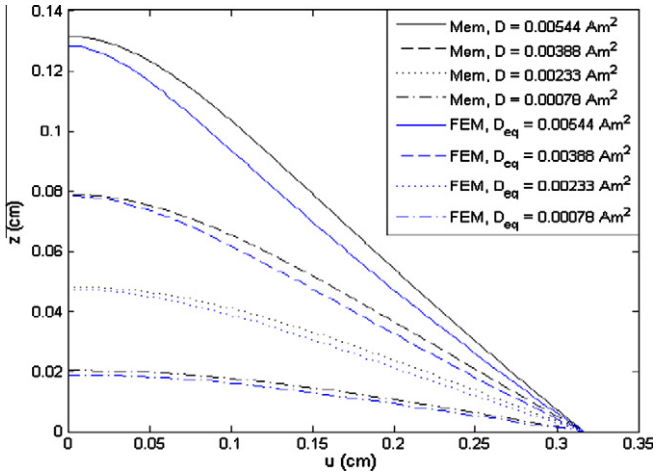

Fig. 6. Comparison of displacement, analysis vs FEM. In this graphic u is the position along the film radius, and z is the vertical displacement.

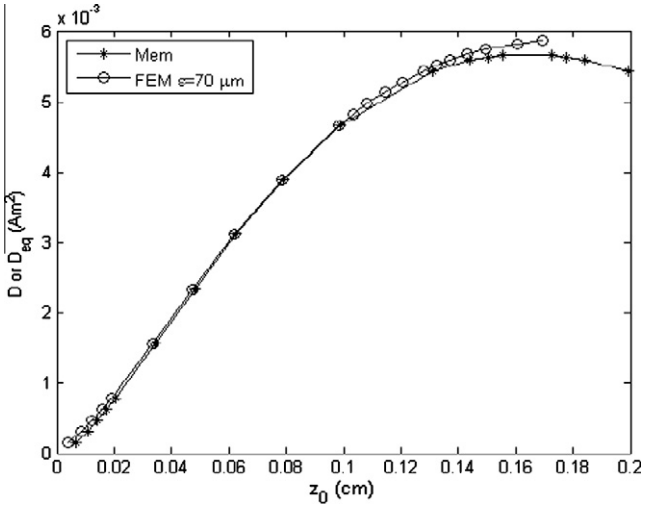

Fig. 7. Comparison of the z-displacement at the center of the film for the two methods as a function of dipole strength. This particular FEM result used a film thickness of $t_f = 70$ μm.

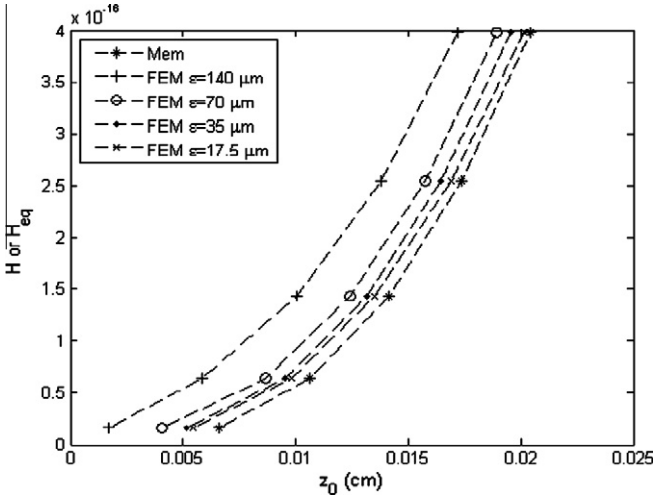

Fig. 8. This graphic compares the FEM results, with different film thicknesses, to the analytical approximation. The displacement is taken at the center of the film. As the thickness decreases, the FEM results converge to the analytical membrane approximation.

although not exact for numerous reasons. The results are not expected to match exactly because the analytical approximation employs the membrane approximation, i.e. no resistance to bending, and as discussed above the magnetic field created by a small ring only approximately matches the dipole field used in the analytical approximation. Another reason for mismatch is the finite film thickness used in the finite element simulations. In order to quantify this, several different film thicknesses were investigated. In Fig. 8 finite element results are compared to the analytical approximation for several different film thicknesses. As the film thickness is decreased, the finite element results converge to the analytical approximation. This provides a good verification of the finite element procedure. If the membrane model is assumed to be the exact solution the error of the FEM model is: 37.0% for $t_f = 140$ μm, 17.1% for $t_f = 70$ μm, 9.7% for $t_f = 35$ μm and 6.7% for $t_f = 17.5$ μm.

5. Conclusions

A finite element algorithm for computing the magnetically driven displacement of a magnetoelastic film was developed. This finite element model combines two established techniques, implicit solution of the Cauchy equation of motion using $H(Grad)^3$-conforming finite elements for the mechanics, and implicit solution of the low-frequency Maxwell's equations using a mixed $H(Curl)$–$H(Div)$ formulation. The two finite element formulations are operator split in time, and coupled by adding the Maxwell stress tensor to the Cauchy stress tensor for the total stress tensor. The algorithm is reminiscent of an approach used for magnetohydrodynamics, the key difference is that the Mooney–Rivlin hyperelastic material model is used for the material constitutive relation, hence at every time step a nonlinear system of equations must be solved.

The finite element algorithm is inherently three-dimensional and designed for transient simulations. However since there is a lack of analytical test problems for full three-dimensional transient solution, the finite element algorithm was compared to a previously developed analytical solution to a two-dimensional steady-state analysis of a circular magnetoelastic film immersed in a dipole field. The analytical solution is based on the membrane approximation. By construction the finite element algorithm must have a finite thickness film, and it is shown that as the film thickness is decreased the finite element solution converges to the analytical membrane approximation, thus providing a good verification of the finite element algorithm.

References

[1] E. Quandt, A. Ludwig, Magnetostrictive actuation in microsystems, Sensors Actuat. 81 (2000) 275–280.
[2] C. Grimes, K. Ong, K. Loiselle, P. Stoyanov, D. Kouzoudis, Y. Liu, C. Tong, F. Tefiku, Magnetoelastic sensors for remote query environmental monitoring, Smart Mater. Struct. 8 (1999) 639–646.
[3] D. Kouzoudis, C. Grimes, The frequency response of magnetoelastic sensors to stress and atmospheric pressure, Smart Mater. Struct. 9 (2000) 885–889.
[4] D. Kouzoudis, C. Grimes, Remote query fluid flow velocity measurement using magnetoelastic thick film sensors, J. Appl. Phys. 87 (9) (2000) 6301–6303.
[5] D. Steigman, Equilibrium theory for magnetic elastomers and magnetoelastic membranes, Int. J. Nonlinear Mech. 39 (2004) 1193–1216.
[6] S.V. Kankanala, N. Triantafyllidis, On finitely strained magnetorheological elastomers, J. Mech. Phys. Solids 52 (2004) 2869–2908.
[7] R. Bustamante, A. Dorfman, R.W. Ogden, On variational formulations in nonlinear magnetoelastics, Math. Mech. Solids 13 (2008) 725–745.
[8] J.E. Marsden, T.J.R. Hughes, Mathematical Foundations of Elasticity, second ed., Dover Publications, New York, 1983.
[9] J.D. Jackson, Classical Electrodynamics, second ed., Wiley, New York, 1975.
[10] R.N. Rieben, D.A. White, B.K. Wallin, J.M. Solberg, An arbitrary Lagrangian–Eulerain discretization of MHD on 3D unstructured grids, J. Comput. Phys. 226 (2007) 534–570.
[11] M. Barham, D.J. Steigman, M. McElfresh, R.E. Rudd, Finite deformation of a pressurized magnetoelastic membrane in a stationary dipole field, Acta Mech. 191 (2007) 1–19.
[12] Z. Ren, F. Bouillault, A. Razek, A. Bossavit, J.C. Verite, A new hybrid model using electric field formulation for 3d eddy current problems, IEEE Trans. Mag. 26 (2) (1990) 470–473.
[13] A. Bossavit, J.C. Verite, The TRIFOU code: solving the 3d eddy current problems by using H as the state variable, IEEE Trans. Mag. 19 (6) (1983) 2465–2470.
[14] A. Bossavit, Computational Electromagnetism: Variational Formulation, Complementarity, Edge Elements, Academic Press, New York, 1998.
[15] O. Biro, K. Preis, On the use of the magnetic vector potential in the finite element analysis of three-dimensional eddy currents, IEEE Trans. Mag. 25 (4) (1989) 3145–3159.
[16] O. Biro, K. Preis, W. Renhart, K. Richter, G. Vrisk, Performance of different vector potential formulations in solving multiply connected eddy current problems, IEEE Trans. Mag. 26 (2) (1990) 438–441.
[17] C. Bryant, C. Emson, C. Trowbridge, A comparison of Lorentz gauge formulations in eddy current problems, IEEE Trans. Mag. 26 (2) (1990) 430–433.
[18] R. Rieben, D. White, Verification of high-order mixed finite element solution of transient magnetic diffusion problems, IEEE Trans. Mag. 42 (1) (2006) 25–39.
[19] K. Fujiwara, Y. Okada, T. Nakata, N. Takahashi, Improvements in the $t - \omega$ method for eddy current analysis, IEEE Trans. Mag. 24 (1988) 94–97.
[20] D.A. White, Using the Sherman–Morrison–Woodbury formula for coupling external circuits with FEM for eddy current problems, IEEE Trans. Mag. 45 (10) (2009) 3915–3918.
[21] D. Arnold, Compatible Spatial Discretization IMA. Volumes in Mathematics and its Applications, Springer, 2006.
[22] P. Castillo, J. Koining, R. Rieben, M. Stowell, D. White, Discrete differential forms: a novel methodology for robust computational electromagnetics, Technical Report UCRL-ID-151522, Lawrence Livermore National Laboratory, Center for Applied Scientific Computing, January 2003.
[23] P. Castillo, R. Rieben, D. White, FEMSTER: An object oriented class library of higher-order discrete differential forms, ACM Trans. Math. Software 31 (4) (2005) 425–457.
[24] M. Brezina, C. Tong, R. Becker, Parallel algebraic multigrid for structural mechanics, SIAM J. Sci. Comput. 27 (2006) 1727–1741.
[25] V. Hensen, U. Yang, BoomerAMG: a parallel algebraic multigrid solver and preconditioner, Appl. Numer. Math. 41 (2002) 155–177.
[26] Z. Kolev, P. Vassilevski, Parallel auxiliary space AMG for $H(curl)$ problems, J. Comput. Math 27 (2009) 604–623.